Preprints (www.preprints.org) | NOT PEER-REVIEWED | Posted: 12 April 2021 doi:10.20944/preprints202104.0319.v1

Article

Influences of CO_2 on the Microstructure in Sheared Olivine Aggregates

Huihui Zhang [1,3], Ningli Zhao [2], Chao Qi [1], Xiaoge Huang [1,*] and Greg Hirth [2]

[1] Institute of Geology and Geophysics, Chinese Academy of Sciences, Beijing 100029, China; zhanghuihui@mail.iggcas.ac.cn (H.Z.); qichao@mail.iggcas.ac.cn (C.Q.)
[2] Department of Earth, Environmental and Planetary Sciences, Brown University, Providence, RI 02906, USA; ningli_zhao@brown.edu (N.Z.); greg_hirth@brown.edu (G.H.)
[3] University of Chinese Academy of Sciences, Beijing 100049, China
* Correspondence: xghuang@mail.iggcas.ac.cn; Tel.: +010 82998429

Abstract: Shear deformation of a solid-fluid, two-phase material induces a fluid segregation process that produces fluid-enriched bands and fluid-depleted regions, and a crystallographic preferred orientation (CPO) characterized by girdles of [100] and [001] axes sub-parallel to the shear plane and a cluster of [010] axes sub-normal to the shear plane, namely the AG-type fabric. Based on experiments of two-phase aggregates of olivine + basalt, a two-phase flow theory and a CPO-formation model were established to explain these microstructures. Here, we investigate the microstructure in a two-phase aggregate with supercritical CO_2 as the fluid phase and examine the theory and model, as CO_2 is different from basaltic melt in rheological properties. We conducted high-temperature and high-pressure shear deformed experiments at 1 GPa and 1100ºC in a Griggs-type apparatus on samples made of olivine + dolomite, which decomposed into carbonate melt and CO_2 at experimental conditions. After deformation, CO_2 segregation and an AG-type fabric occurred in these CO_2-bearing samples, inconsistency with basaltic melt-bearing samples. The SPO-induce CPO model was used to explain to the formation of the fabric. Our results suggest that the influences of CO_2 as a fluid phase on the microstructure of a two-phase olivine aggregate is similar to that of basaltic melt and can be explained by the CPO-formation model for the solid-fluid system.

Keywords: olivine aggregates; CO_2; crystallographic preferred orientation; AG-type fabric

1. Introduction

In the mantle of the Earth, deformation often occurs in regions where the melt is produced and transported, such as plate boundaries, plumes, intra-plate rifts, and boundary layers. Deformation and melt transport, including melt migration and segregation, are strongly coupled in partially molten rocks, as evidenced by field observations [1], laboratory experiments [2], and theoretical analyses [3]. Significantly, melt spontaneously localizes into melt-enriched bands oriented ~20° to the shear plane, antithetic to the shear direction in partially molten rocks deformed in general and torsional shear [4-7]. The formation of melt-enriched bands is predicted and modeled by the two-phase flow theory with anisotropic viscosity [3, 8-9]. Moreover, shear deformation of partially molten, olivine aggregates produces a crystallographic preferred orientation (CPO), which is characterized by a cluster of [010] axes sub-normal to the shear plane and girdles of [100] and [001] axes sub-parallel to the shear plane [2, 10]. This CPO, often referred to as AG-type fabric [11], forms due to the development of a shape preferred orientation (SPO), while the grain shape is crystallographically controlled in partially molten olivine aggregates [10].

Deformation-induced microstructural features in partially molten rocks, primarily the re-distribution of melt and the formation of CPOs as introduced above, have mostly been investigated in the solid-fluid system consisting of olivine and basaltic melt [12-14]

© 2021 by the author(s). Distributed under a Creative Commons CC BY license.

Preprints (www.preprints.org) | NOT PEER-REVIEWED | Posted: 12 April 2021 doi:10.20944/preprints202104.0319.v1

or other silicate melt [7]. These fluid phases have low dihedral angles, 30-50° [15-17], relatively high viscosities, > 100 Pa·s for basaltic melt at 1473 K [7], and high solubility for the solid phase [18, 19]. Upon those common properties of the fluid phases, previous theory for melt distribution and mechanism for CPO formation were built. However, whether the theory and mechanism apply to fluid phases with very different properties is yet to be examined. Supercritical carbon dioxide (CO_2), a fluid state of carbon dioxide at or above its critical temperature and pressure, is a fluid phase suitable for the examination. A laboratory study found the dihedral angles in the olivine - CO_2 system are generally in excess of 60º and sometimes up to 90º [20]. A model extrapolated from laboratory measurements suggests that the viscosity of CO_2 is lower than 0.1 mPa·s at 1 GPa and 900 K [21]. Conductivity experiments carried out on peridotite show that adding carbonate melt significantly increases the electrical conductivity [22], indicating that presence of carbonate melt enhances the transport properties. Moreover, CO_2 and carbonate melt are also of importance for the dynamics of the mantle. With the mantle being the largest carbon reservoir, carbon cycles between the mantle and the atmosphere via volcanic activities and subduction [23], where severe deformation occurs. In the upper mantle, carbon exists as CO_2 or carbonate melt [24]. At certain geological conditions, carbonate melt will decompose into CO_2, which can be held stable in the lithosphere [25]. Thus, the influence of CO_2 and carbonate melt on the microstructures in olivine aggregates not only aids the understanding of the microstructural evolution of partially molten rocks, but also benefits the study of carbon transportation in the mantle.

In the present paper, we conducted laboratory deformation experiments on olivine + CO_2 aggregates at high temperature and pressure. Detailed microstructural analyses of sheared samples provide observations on the distribution of CO_2 and the development of CPOs. In this contribution, we focus on the CPOs. A comparison between CPOs observed in this study and those reported in olivine + basalt samples reveal the mechanism for CPO formation in this solid-fluid, two-phase system.

2. Experimental methods

2.1. Sample Preparation

Samples were fabricated from mixtures of powders of olivine, 3 wt % clinopyroxene (CPx, with ~8 wt% of orthopyroxene; [26]) and 9 wt% dolomite. Olivine and CPx crystals were hand-picked from a lherzolite xenolith (Damaping, Hebei, China; [27]). The composition of the dolomite is $CaMg(CO_3)_2$. Olivine, CPx, and dolomite were separately ground in an agate motor and sieved to a particle size of < 32 μm. Powders of olivine and CPx were subsequently baked in a furnace for 20 hours at 850ºC and an oxygen fugacity set by flowing CO and CO_2 at a ratio of 1:1, which is within the stability field of natural olivine ($f_{O2} = 10^{-14}$ Pa). Then powders were mechanically mixed.

Each sample was prepared by cold-pressing ~0.1 g of the mixture into a nickel can between two alumina pistons beveled at 45º. The details of the experimental assembly are illustrated in Figure 1a. Before hot-pressing, cold-pressed samples were stored in a vacuum oven at 110ºC for more than 6 hours. Cold-pressed samples were then hot-pressed at 1100ºC and a confining pressure of 1 GPa for 17-18 hours in a Griggs-type apparatus.

Preprints (www.preprints.org) | NOT PEER-REVIEWED | Posted: 12 April 2021 doi:10.20944/preprints202104.0319.v1

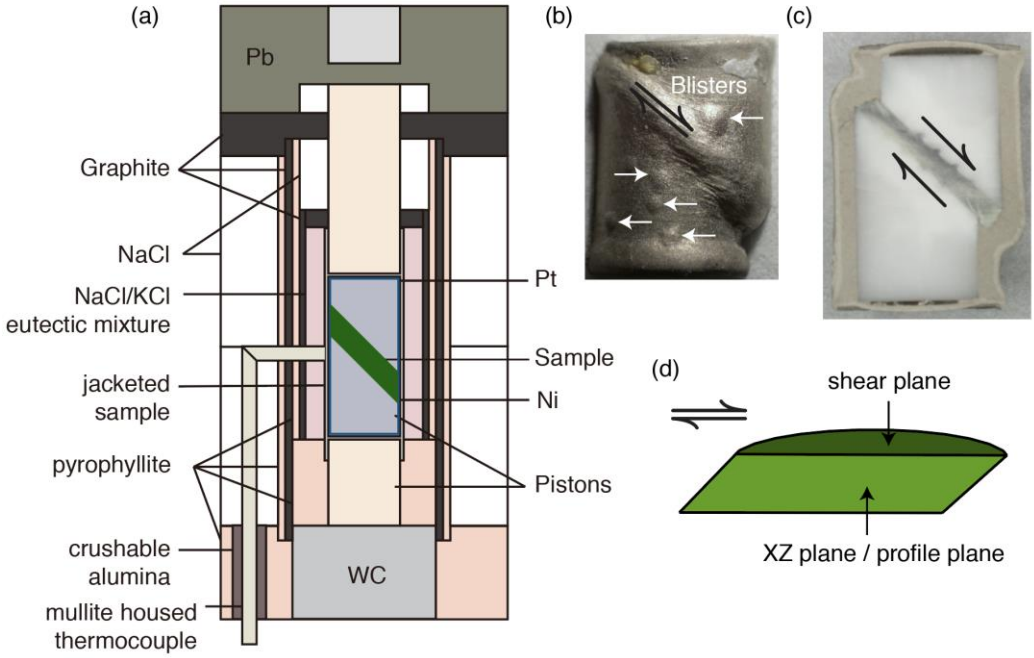

Figure 1. (a) A sketch of the experimental assembly. (b) A photo of a deformed sample. Blisters on the surface of the Ni jacket are marked by white arrows. (c) A photo of a sample cut through the profile plane. (d) The schematic illustration of the shear plane and profile plane.

2.2. Deformation experiments

Immediately after hot-pressing, samples were deformed at 1100ºC and 1 GPa. Two experiments (W2264 and W2266) were carried out at a constant axial displacement rate of 7.5×10^{-5} mm/s to a shear strain of $\gamma \approx 3$. After deformation, one experiment (W2266) was then annealed for 10 hours at 1100ºC and 1 GPa. A strain-rate-stepping experiment (W2263) was carried out at axial displacement rates of 7.5×10^{-5} mm/s, 1.9×10^{-5} mm/s, 1.9×10^{-4} mm/s, and 7.5×10^{-5} mm/s to a total shear strain of $\gamma \approx 5$.

At the end of each experiment, the sample was first quenched to 800ºC then temperature was decreased to 300ºC in less than 10 min. The confining pressure was decreased while maintaining a differential stress less than 100 MPa at 300ºC to minimize unloading cracks. When the confining pressure decreased to 500 MPa, we started to decrease temperature again. With the confining pressure decreasing to 0 MPa, the temperature was gradually lowered to the temperature of the cooling water (19ºC).

2.3. Mechanical data processing

Axial displacement, load, temperature and confining pressure data were collected every second in our apparatus. Axial displacement rate was multiplied by $\sqrt{2}$ and divided by the measured thickness of samples, to obtain the shear strain rate. Equivalent strain rate was obtained by dividing shear strain rate by $\sqrt{3}$. The thinning of specimens resulted in a small increase of shear strain rate even with an imposed constant axial displacement rate. We obtained a linear correlation between the specimen thickness and shear strain, which was incorporated into the calculation of shear strain rate. Comparison of hot-pressed and deformed specimens indicates that sample thickness decreases from ~1.3 mm to ~0.9 mm after a shear strain of $\gamma = 3$, which increases shear strain rate by 40% (Appendix Figure A1).

Axial load was converted to axial differential stress by dividing the axial load by the area of the horizontal cross section of the pistons. Axial differential stresses were corrected for force contributions from assembly friction by subtracting the friction estimated by an intercept of two linear fits of force-displacement curves just before and just after the specimen "hit point" [28]. Shear stress was calculated by dividing the differential stress by 2.

Preprints (www.preprints.org) | NOT PEER-REVIEWED | Posted: 12 April 2021 doi:10.20944/preprints202104.0319.v1

Equivalent stress was then obtained by applying a factor of $\sqrt{3}$ to the shear stress. The accuracy of stress data is estimated to be ± 5 MPa.

2.4. Microstructure analysis

After each deformation, the nickel jacket was peeled off, and alumina pistons were cut off. Each sample was cut perpendicular to the shear plane (referred to as "profile plane" as illustrated in Figure 1d). The sample section was dry-polished on a series of diamond lapping films down to 0.5 μm. To protect deformation microstructures of the highly porous samples, the usage of water, ethanol or any fluids was avoided during mechanical polishing. After dry polishing, the sample was polished with 0.02 μm SiO2 non-crystallizing colloidal silica for ~4 hours. In two samples (W2263 and W2264), a section was also cut parallel to the shear plane (Figure 1d) and polished in the same manner as described above.

Polished sections prepared for analysis by electron backscatter diffraction (EBSD). To obtain crystallographic orientation data, high-resolution orientation maps with a step size of 0.5 μm were collected for all sections using a Zeiss Sigma field emission SEM equipped with an Oxford Instruments Nordlys Nano EBSD detector and a Tescan MIRA3 LMU field emission scanning electron microscope equipped with an Oxford Instruments Nordlys-Max2 EBSD detector (only for W2264). Raw orientation data were processed with HKL Channel5 software, including removal of single misindexed points, assigning unindexed points the average orientation of neighboring grains, and removal of systematic misindexed points, as outlined in previous studies [29, 30].

Grains were constructed from processed orientation data using the MTEX toolbox [31] in MATLAB. Grain boundaries were drawn where neighboring pixel misorientations exceeded 10°. No extrapolation of orientation data was applied in MTEX, because the data were already processed by the HKL Channel5 software. Grain size was determined by applying a factor of $4/\pi$ [32] to the equivalent diameter of a circle with the area of each grain in cross section. In the analysis of the average grain size for a map, grains containing less than 4 pixels or lying on the edge of the map were excluded.

To analyze the grain shape, each grain was fit with an ellipse to obtain its aspect ratio and the orientation of the long axis using MTEX toolbox [31]. Grains with an area of less than 2 μm^2 were excluded, because they do not contain enough pixels to derive reliable values of aspect ratio and slope of the ellipse. Then the shape preferred orientation (SPO) is illustrated by a rose diagram, and the distribution of aspect ratios is illustrated by a histogram. An analysis of the SPOs in grains grouped with respect to their crystallographic orientations were performed following the methods described in Qi et al. [10] in the profile and shear planes.

Orientation distributions were generated from the mean orientations of at least 500 grain with a half-width angle of 10° using the MTEX toolbox in MATLAB [33, 34]. For easy comparison with previous studies, orientation data were rotated so that the sense of shear is top to the right. To quantify the strength of the CPOs, both the J-index [35] and the M-index [36] were used.

After EBSD analysis, the sample was etched in phosphoric acid for 45 minutes to highlight grain boundaries in preparation for analysis by scanning electron microscopy (SEM). After coating the sections with > 8 nm thick carbon, backscattered electron images were collected using a Zeiss Sigma field emission scanning electron microscope at an accelerating voltage of 15 kV. The CO_2 fraction for each sample were estimated in SEM images by assuming CO_2 occupied all the pockets.

2.5. Composition analysis

Electron microprobe analyses (EMPA) were performed on a SXFive. Samples were analyzed using an accelerating voltage of 15 kV, a beam current of 20 nA and a focused beam. We have no direct method of analyzing the concentration of CO_2 in partial melts,

Preprints (www.preprints.org) | NOT PEER-REVIEWED | Posted: 12 April 2021 doi:10.20944/preprints202104.0319.v1

as they did not quench to a glass. The CO_2 in the melts may be estimated by difference between 100% and the observed microprobe totals [37].

3. Results

3.1. Starting materials

In our samples, 9 wt% dolomite was added to the olivine aggregates as a CO_2 source. At our experimental conditions (1100ºC and 1GPa), dolomite thermally decomposes and melts, producing supercritical CO_2 and carbonate melt [38, 39]. After samples (both hot-pressed and deformed) were removed from the apparatus, many "blisters" started to appear on the surface of the Ni jacket (Figure 1b). Piercing through the Ni jacket with sample submerged into ethanol, gas bubbles were released from the blisters for several minutes – indicating CO_2 was successfully encapsuled in the assembly by the jacket at our experimental conditions.

The presence of CO_2 was also evidenced by the microstructures presented in Figure 2a and b. Voids (Figure 2b) located at grain boundaries and junctions are interpreted as CO_2 fluid, in accordance with the results of [40]. Carbonate melt is homogeneously distributed in the hot-pressed sample. Most CO_2 and melt pockets are located at triple junctions and grain boundaries of the solid phase, with no melt-preferred orientation observed. Many "pluck-outs" are observed in Figure 2b. These pluck-outs should be large CO_2 pockets with carbonate melt around them, which were damaged during polishing. By image analysis, the porosity in the hot-pressed sample is approximately 7 %, including the CO_2 and pluck-outs.

Grain size of the hot-pressed sample roughly fits to a lognormal distribution, with a mean grain size of 5.7 μm, as illustrated in Figure 2c. The CPO is approximately random with a M-index of 0.017, as illustrated in Figure 2d. For water content, the polycrystal of the hot-pressed sample (including grain boundaries) contained approximately 9 ppm H_2O by weight (FTIR result presented in Appendix A2). Chemical compositions of olivine, CPx and carbonate melt were also analyzed by electron microprobe (Appendix Table A1 for details).

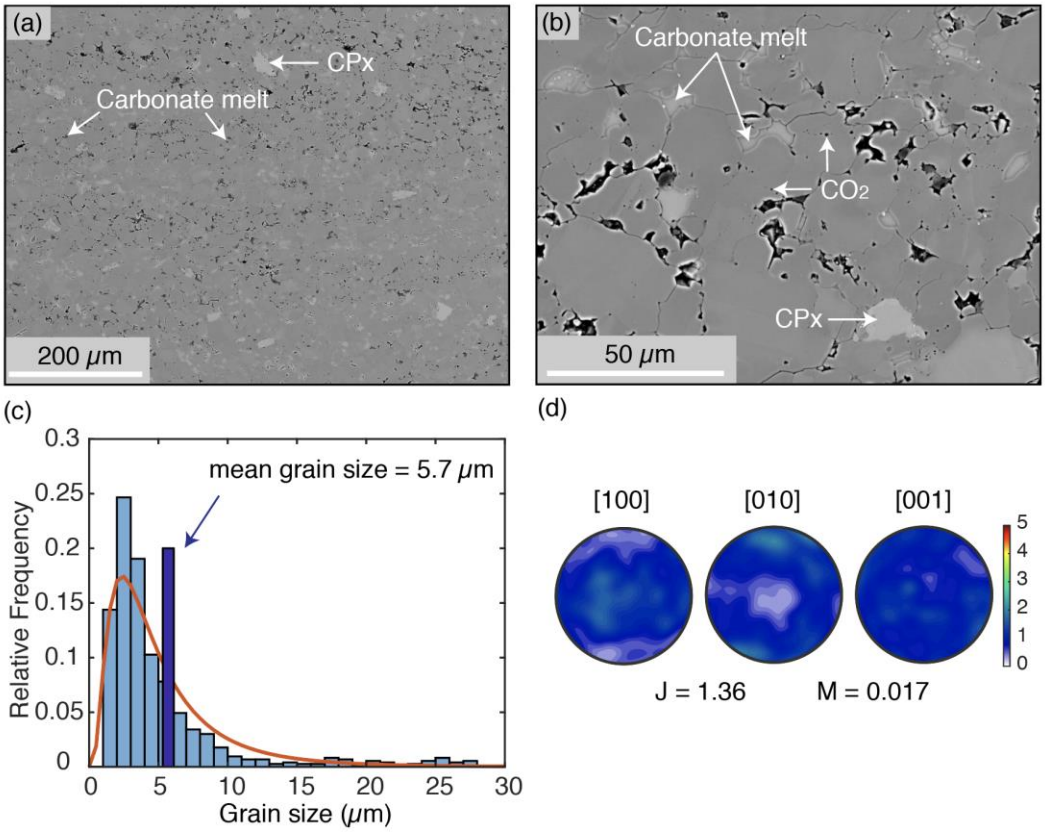

Preprints (www.preprints.org) | NOT PEER-REVIEWED | Posted: 12 April 2021 doi:10.20944/preprints202104.0319.v1

Figure 2. The backscattered electron (BSE), grain size, and crystallographic orientations of the hot-pressed sample (W2261). (a) and (b) BSE images. The majority of the grey phase is olivine, with small contrast caused by orientation. The oblate and rotund voids are CO_2 (formerly CO_2-filled). The voids at triple junctions are interpreted to be CO_2 and surrounding the carbonate melt, removed during polishing. A few CPx grains (light grey) are observed. (c) Frequency distribution of grain size. The red curve is a lognormal distribution of grain size. The mean is noted on the histogram. (d) Pole figures of crystallographic orientations. Color scale indicates the multiples of a uniform distribution (MUD).

3.2. Mechanical data

The sample conditions and deformation conditions including the imposed strain rate, stress, and strain at the end of each experiment are summarized in Table 1. As described in the Methods section, samples were hot-pressed and then immediately deformed. After deformation, the sample was flattened normal to the imposed shear direction. Therefore, the strain rate of an experiment was calculated using imposed displacement rate and interpolation of the sample thickness. No slip between pistons and samples was observed (Figure 1c).

Graphs of equivalent stress plotted against equivalent strain are presented in Figure 3. All the curves for experiments showed a rapid stress rise to a peak stress at an approximate equivalent strain of ~0.2, followed by a steep drop to a more slowly changing stress with increasing strain. The experiments in Figure 3a were carried out at the same equivalent strain rate ~ 6.0×10^{-5} s^{-1} and the equivalent stresses were around 175 MPa. At the end of the experiment W2264, the tungsten carbide piston above the sample assembly cracked and influenced the stress data (dashed lines), so we used mechanical data (grey circle) right before it happened. The shear strain measured using external LVDT ($\gamma = 3.2$) is consistent with the offset of the piston (Figure 1c) after correction of contribution of the elastic portion of the shear strain ($\gamma = 2.6$). Four strain-rate steps were performed during the rate-stepping experiment. During each strain-rate step, when the stress reached a steady state, the strain rate was changed to next step. Although strain-rate steps were taken in an experiment, a flow law is not derived based on only four data points, because the number of parameters in a flow law will render the problem underdetermined and that the discussion of a flow law for our aggregate consisting of olivine, CPx, CO_2 and carbonate melt is beyond the scope of this paper.

Table 1. Summary of Experiments.

No.	Experiment Type	Measured Porosity	Axial Displacement Rate (mm/s)	Equivalent Strain Rate (/s)	Equivalent Stress (MPa)	Shear Strain	Equivalent Strain	Grain Size* (μm)	Thickness* (mm)
W2261	Hot-pressing	7.0 %						5.7	
W2263	Rate stepping	5.8 %	7.5×10^{-5}	6.0×10^{-5}	131	1.8	1.0		
			1.9×10^{-5}	1.6×10^{-5}	61	3.0	1.7		
			1.9×10^{-4}	1.9×10^{-4}	237	4.4	2.5		
			7.5×10^{-5}	8.0×10^{-5}	147	4.9	2.8	4.5	0.74
W2264	Constant rate	7.2 %	7.5×10^{-5}	5.9×10^{-5}	178	3.2	1.8	5.8	0.88
W2266	Annealing	6.5 %	7.5×10^{-5}	6.7×10^{-5}	174	3.2	1.8	7.3	0.77

*: Grain size and thickness are measured after the experiment.

Preprints (www.preprints.org) | NOT PEER-REVIEWED | Posted: 12 April 2021 doi:10.20944/preprints202104.0319.v1

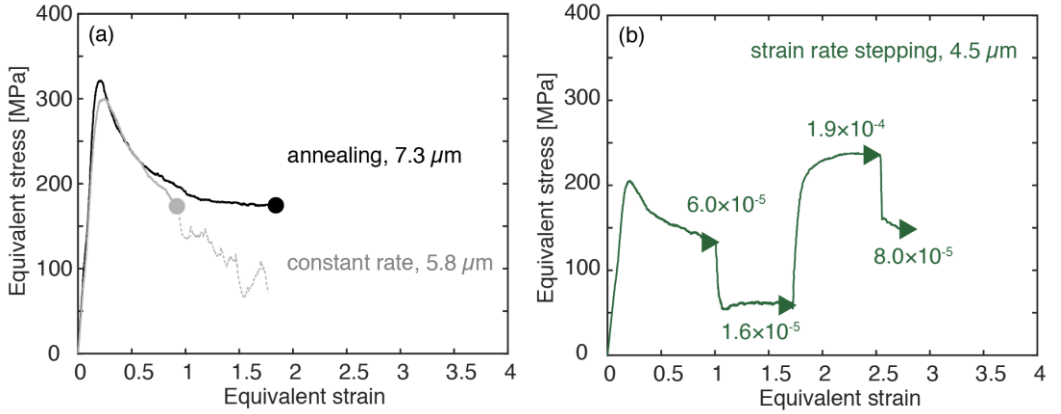

Figure 3. Mechanical data for deformation experiments on CO_2-bearing samples with final grain size and experiment type noted for each curve. (a) Equivalent stress versus equivalent strain plots for general shear experiments conducted at the strain rate of ~ 6.0×10^{-5} s^{-1}; circles illustrated where mechanical data are determined. The grey and black lines illustrate results for experiments (W2264 and W2266, respectively). Sample W2266 was annealed for 10 hours at 1 GPa and 1100ºC after deformation. At the end of the experiment W2264, the deformation piston cracked and influenced the stress data (dashed lines), so we used mechanical data (grey circle) right before it happened. (b) Equivalent stress versus equivalent strain plot for rate-stepping experiment (W2263) deformed in general shear. Strain rates (s^{-1}) are noted for each step.

3.3. Distribution of CO_2

Here, detailed microstructural observations of a deformed sample (W2264) are presented. As illustrated in Figure 4, CO_2 and carbonate melt were highlighted as pores in the micrographs of the etched polished section. The size and distribution of the pores represent the redistribution of CO_2 induced by shear deformation. The size of the pores, that is, the size of CO_2 and the surrounding melt, ranges from a couple of microns to close to the lower limit of the olivine grain size. The smaller pores, probably single CO_2 pockets, are sparsely and homogenously distributed at olivine triple junctions and along the olivine grain boundaries as isolated "bubbles". The presence of CO_2 pocket at triple junctions arises because of a relatively high fraction of CO_2 (> 5 %), which is consistent with the calculations of von Bargen and Waff [46].

The distribution of CO_2 and melt was dramatically changed after deformation. CO_2 segregated into high-porosity bands, that is, CO_2-enriched bands, orienting ~20º from the shear plane, synthetic to the imposed shear direction. CO_2-enriched bands, occurred across the entire section, are separated by low-porosity regions, that is, CO_2-depleted regions. Within the bands, pores are interconnected. The CO_2-enriched bands are ~30-μm wide, while the CO_2-depleted regions are ~100-μm wide. In compared with the CO_2, the carbonate melt was mostly tended to aggregate at the boundary between piston and sample during the deformation process (The distribution showed in Appendix A3). The analysed regions of microstructures and CPO were from the center of samples, so we focus on the influence of the presence of the CO_2.

Preprints (www.preprints.org) | NOT PEER-REVIEWED | Posted: 12 April 2021 doi:10.20944/preprints202104.0319.v1

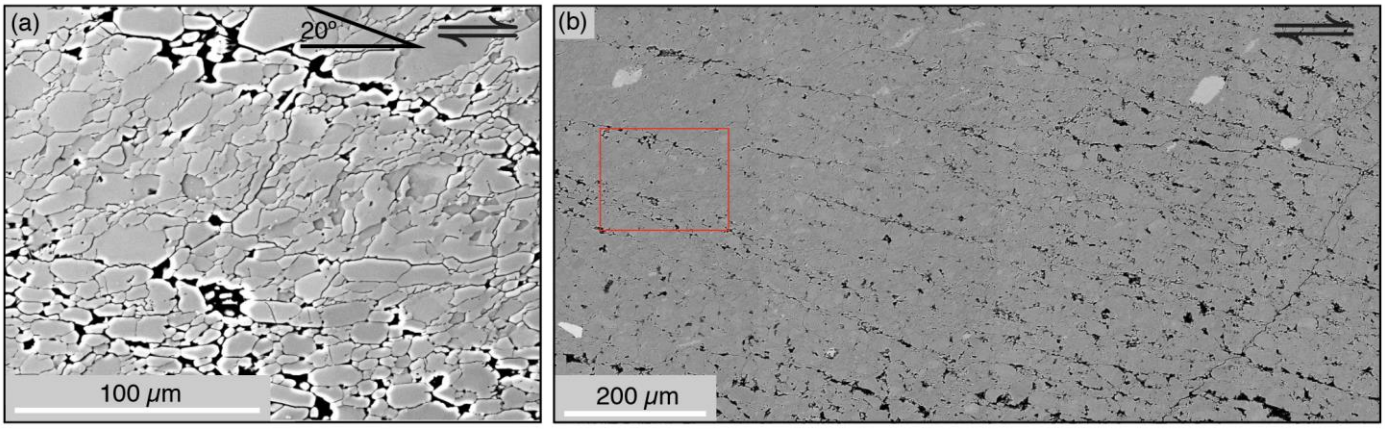

Figure 4. BSE micrographs of the etched surface of deformed sample, W2264. (**a**) A close look at CO_2-enriched bands and the CO_2-depleted region in between. (**b**) A broad view of deformed sample. The red frame indicates where the region of (**a**) is picked. The diopside (white) set in the olivine grains (gray). The tubules (black) are formerly CO_2-filled.

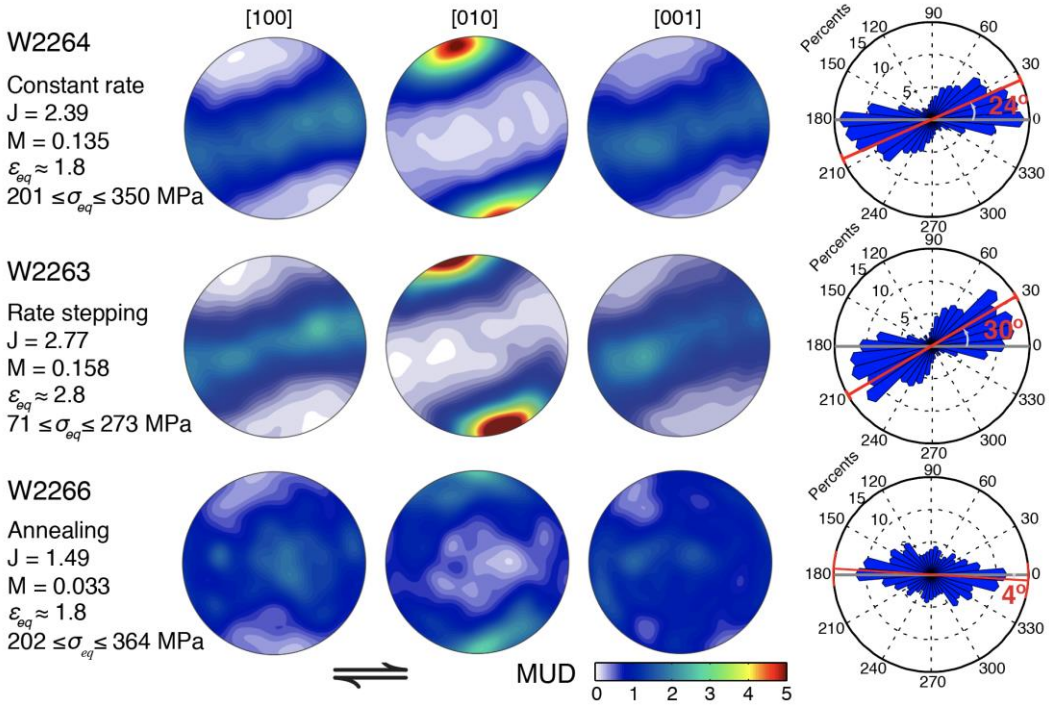

Figure 5. CPOs and SPOs in the profile plane of 3 samples. From top to bottom are the sample deformed at a constant rate, W2264, the sample deformed at different strain rate steps, W2263, and the sample annealed for 10 hrs after deformation. Pole figures and rose diagrams are processed from grains with grain areas greater than 2 μm2 and aspect ratios greater than 1.2. J-index, M-index, were calculated for each crystallographic fabric. The angle between the SPO and the shear direction is noted on each rose diagram.

3.4. Crystallographic preferred orientation and shape preferred orientation

To examine the crystallographic preferred orientation and shape preferred orientation of olivine grains in our CO_2-bearing samples, pole figures highlighting the CPOs and rose diagrams quantifying the SPOs are presented in Figure 5. In both deformed samples, CPOs are characterized by girdles of [100] and [001] axes sub-parallel to the shear direction, and strong point maxima of [010] axes sub-perpendicular to the shear plane, namely the AG-type fabric [11]. The fabric is rotated 20 to 30º, antithetic to the shear direction, from [010] axes being normal the shear plane. With equivalent strain increasing from 1.8 to 2.8, the strength of the fabric increases slightly, with the J-index increases from 2.39 to 2.77 and the M-index increases from 0.135 to 0.158. In both deformed samples, the long axes of olivine grains align 27 ± 3° from the shear plane, antithetic to the shear direction.

Preprints (www.preprints.org) | NOT PEER-REVIEWED | Posted: 12 April 2021 doi:10.20944/preprints202104.0319.v1

The annealed sample is very different from the two deformed samples in terms of CPO and SPO. The CPO is characterized by a diffused cluster of [010] axes normal to the shear plane, and almost random distributed [100] and [001] axes. This CPO is very weak, with a J-index of 1.49 and M-index of 0.033. The long axes of olivine grains align roughly in the shear plane.

4. Discussion

4.1. A comparison with the CPOs in olivine + basalt

In the previous section, our observations on sheared samples revealed an AG-type fabric in CO_2-bearing olivine aggregates. Comparing with the A-type fabric, typically occurred in anhydrous olivine aggregate sheared at similar conditions to this study [41], this fabric is characterized by two key features: (1) girdles of [100] and [001] axes at a low angle to the shear plane, with a strong [010] maxium nomal to the girdle, and (2) antithetic rotation of the fabric with respect to the shear plane. The CPO is very similar to the CPOs observed in sheared partially molten rocks of olivine and basalt [4, 10], except for that the weakly aligned, shear-direction-normal [100] axes in the shear plane were not observed in our samples. Qi et al. [10] proposed a melt-assisted, SPO-induced CPO model to explain the formation of the CPOs in the olivine + basalt samples. Based on the similarities and differences in the CPOs between sheared CO_2-bearing olivine and basaltic melt-bearing olivine, in the following discussions, we examine the applicability of the model to our samples and explain the formation of the CPOs.

4.2. Crystal habit of olivine grains

One key in the SPO-induced CPO model is that the grain shape is crystallographically controlled [42]. Studies of the morphology of olivine grains in an ultramafic melt demonstrate a crystal habit with grain shapes longest parallel to the [001] axis and shortest parallel to the [010] direction [43], which was observed in the partially molten samples analyzed by Qi et al. [10]. However, the crystal habit of olivine grains in the CO_2-bearing samples, that is, a solid-fluid system with supercritical CO_2 and carbonate melt as the fluid phase, is unknown.

To explore the morphology of olivine grains in the CO_2-bearing samples, grain shape and crystallographic orientation were examined for two orthogonal surfaces (profile and shear planes) on a CO_2-bearing sample sheared to a strain of 1.8. In Figure 6, the orientations of crystallographic axes of grains selected based on their grain shape in the section are examined with pole figures, rose diagrams of the orientations of long axes of grins, and histograms of aspect ratios. In the pole figures, light gray girdles and clusters in the background represent the overall CPO observed in this section. The yellow stars indicate the reference orientation for the subset of grains used to make the other plots in this panel. Blue and red dots in the pole figures indicate the orientations of the selected subset of grains. The orientations of these grains lie within 30º to the target orientation. Each grain in a subset is fitted with an ellipse with its long-axis orientation plotted in the rose diagram and aspect ratio plotted in the histogram. This information permits a comparison of the preferred orientations of crystallographic axes with the orientation of long axes of grains.

In the profile plane, [010] axes form strong point maxima sub-perpendicular to the shear plane, so comparisons are only obtained between the relative lengths of grains along [100] and [010] axes (Figure 6a), and between the relative lengths of grains along [001] and [010] axes (Figure 6b). In Figure 6a, [001] axes align subparallel to the shear direction in this subset, and the SPO reveals that the orientation of the long axes is in the same direction as the [001] axes. Therefore, grains are longer along [001] axes than along [010] axes. Similarly, Figure 6b indicates that grains are longer along [100] axes than along [010] axes. In the shear plane, Figures 6c and 6d, the relative lengths along [100] and [001] axes are compared. In both panels, grain shape exhibits a bimodal distribution. The primary mode corresponds with long [001] axes, while the secondary mode corresponds with elongated

Preprints (www.preprints.org) | NOT PEER-REVIEWED | Posted: 12 April 2021 doi:10.20944/preprints202104.0319.v1

[100] axes. This result suggests that grains have similar lengths along [100] and [001] axes, with more grains slightly longer parallel to [001] axes.

Note that this crystal habit is different from that reported in Miyazaki et al. [42], in which forsterite exhibited elongation along [100] axis, or Qi et al. [10], in which San Carlos olivine exhibit elongation along [001] axis. Since the samples consist of olivine, CPx, carbonate melt and CO_2, these compositional differences must lead to differences in the crystal habit.

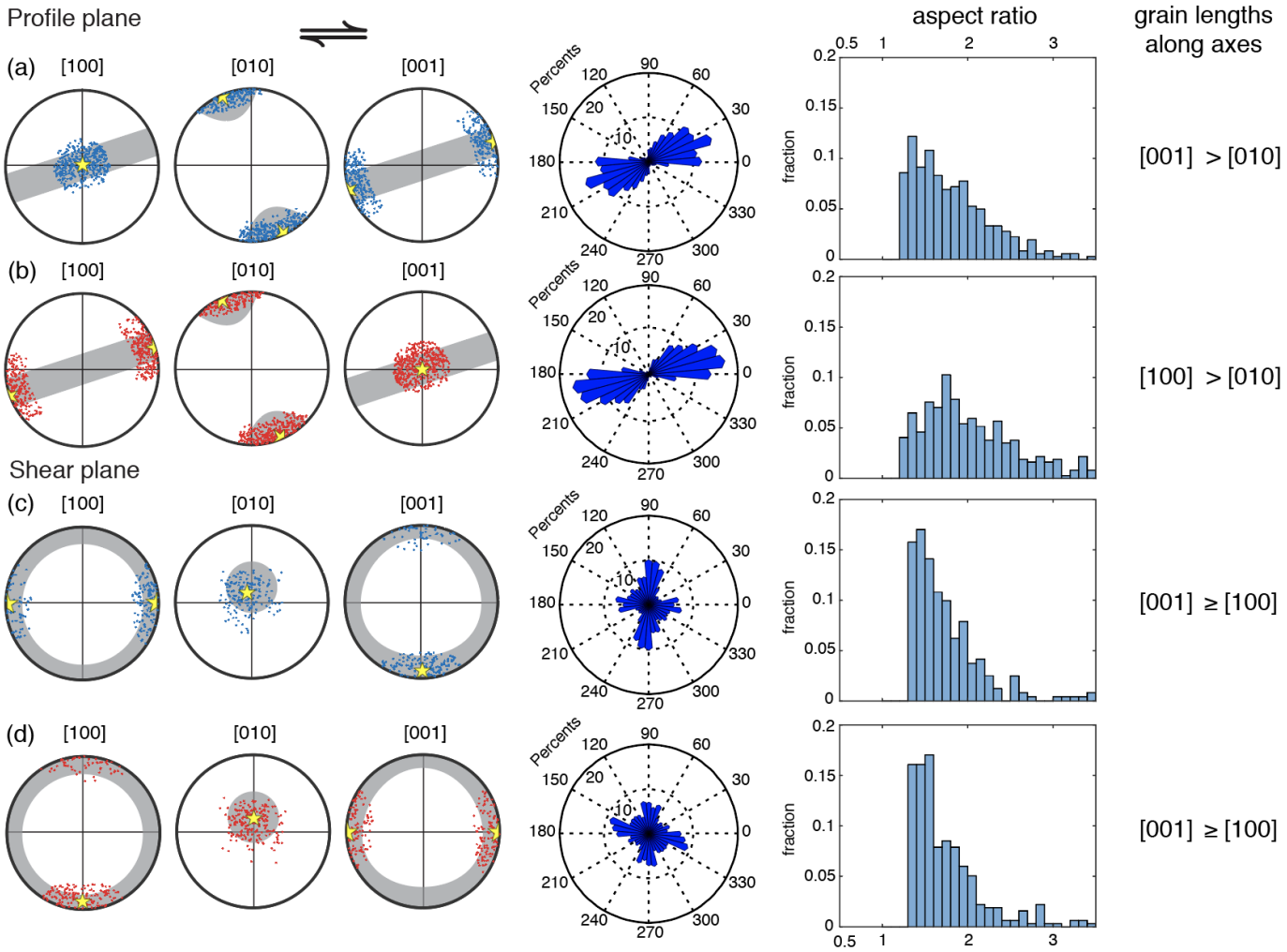

Figure 6. For the deformed sample, W2264, comparison of orientation of crystallographic axes with direction of the long axes of selected subsets of grains. In plots (**a**)–(**d**), the blue and red points in the pole figures indicate the subsets of grains that were selected based on their crystallographic orientations, the rose diagrams show the orientations of the long axes of this subset of grains, and the histograms illustrate their aspect ratios. The gray regions in the pole figures represent the overall CPO, and the yellow stars represent the reference orientation of the subset of grains. In the rose diagrams, the length of each bar corresponds to the fraction of grains with a specific orientation. The relative lengths of grains along the three crystallographic axes are summarized in the far right-hand column. Only grains with aspect ratios greater than 1.2 were used in this analysis.

4.3. SPO-induced CPO model

CPO can be induced by a crystallographically controlled SPO [42]. As elaborated in Qi et al. [10], during simple shear, the long axes of elongated grains are rotated towards the shear direction, which produces a SPO. Then, if the elongated grain shape is crystallographically controlled, the SPO results in a CPO. As demonstrated in the previous subsection, olivine grains are on average shortest along [010] axes and similar in length along [100] and [010] axes. Simple shear of these oblate ellipsoidal grains would align the shortest axes, [010] axes, normal to the local shear plane, resulting a cluster of [010] axes, and

Preprints (www.preprints.org) | NOT PEER-REVIEWED | Posted: 12 April 2021 doi:10.20944/preprints202104.0319.v1

homogeneously distribute the two similarly long axes, [100] and [001] axes, in the local shear plane, resulting in girdles of [100] and [001] axes. The 30º back-rotation observed in both CPO and SPO is consistent with the SPO-induced CPO model.

4.4. Local deformation geometry

Fluid phase segregation occurred in our sheared CO_2-bearing samples, in a very similar way as the melt segregation occurred in sheared olivine + basalt samples. When stress-driven melt segregation occurred, an anastomosing network of melt-enriched bands forms at an angle to the bulk shear plane, synthetic to the bulk shear direction. These melt-enriched low-viscosity bands deform more easily than melt-depleted regions. Because of strain incompatibility at the sample ends, the imposed shear requires the non-band regions to accommodate strain at an angle to the bulk shear plane, rotated antithetically to the imposed shear direction [44]. Similarly, this strain partitioning process must apply to sheared CO_2-bearing samples, where stress-driven phase segregation occurred. Therefore, the counterclockwise rotation of [010] axes from the normal to the shear plane is due to strain partitioning between the CO_2-enriched and CO_2-depleted regions. The [010] axes are normal to the local shear plane, and [100] and [001] axes lie in the local shear plane in the CO_2-depleted portions of a sample, as the bands only take a small fraction of the total volume.

4.5. CPO modification during annealing

Grain size and the CPO of the annealed sample were compared with those of the deformed samples in Table 1 and Figure 5. After annealing, the grain size increased from 5.8 μm to 7.3 μm (increased by 26%) in 10 hrs. Grain growth in this sample is much slower than that in samples of Boneh et al. [45], in which study, 200-μm grains were observed after only four hours of annealing. We infer that the CO_2 pockets distribution in the deformed samples (Figure 4) probably inhibit the rate of grain boundary migration, thus limiting the grain size in the annealed sample. And CO_2-enriched bands were less obvious in the annealed sample (Appendix A4).

The CPO of the annealed CO_2-bearing samples is modified significantly in terms of its strength and its orientation. The M-index decreased from 0.135 to 0.033 after 10 hours of annealing, and the decrease rate is significantly faster than that reported in Boneh et al. [45]. Compared to the deformed samples, the cluster of the [010] axes rotated to become perpendicular to the shear plane. Shape preferred orientation also changed after annealing, with the long axes of olivine grains align roughly parallel to the shear direction (Figure 5). The rotation of the CPO correlate with the rotation of SPO. Currently data is insufficient to explain the changes in the microstructure during annealing, which are dramatically different from the changes in melt-free samples, but the alteration of the interfacial energy due to the existence of fluid/melt phase may significantly affect the annealing behavior.

5. Conclusions

In this study, we investigated the microstructure in sheared CO_2-bearing olivine aggregates. Stress-driven fluid segregation occurred, producing CO_2-enriched bands at ~20º to the shear plane, synthetic to the shear direction. An AG-type fabric was found in sheared samples. [100] and [001] axes form girdles sub-parallel to the shear plane, and [010] axes form a strong cluster sub-normal to the shear plane. A strong correlation exists between the orientation of the gridles and the SPO, indicating that this CPO is developed due to the SPO-induced CPO model. Our study suggests that the CPO-formation mechanism established in the solid-fluid system of olivine + basalt also applies to the solid-fluid system of olivine + CO_2. Degassing of CO_2 from peridotite is an important part of global CO_2 cycling. Our results provide constraints on the microstructures effect of CO_2 on peridotite and the relative of CPO and SPO.

Preprints (www.preprints.org) | NOT PEER-REVIEWED | Posted: 12 April 2021 doi:10.20944/preprints202104.0319.v1

Author Contributions: Conceptualization, X.H. and G.H.; methodology, G.H., N.Z. and H.Z.; validation, H.Z., N.Z., C.Q., X.H. and G.H.; formal analysis and investigation, H.Z., N.Z., G.X., and X.H; resources, H.Z.; data curation, H.Z. and N.Z; writing—original draft preparation, H.Z.; writing—review and editing, N.Z., G.H. and C.Q.; visualization, H.Z., N.Z., and C.Q.; supervision, G.H., C.Q., and X.H.; project administration, G.H. and X.H.; funding acquisition, G.H. and X.H. All authors have read and agreed to the published version of the manuscript.

Funding: This research was funded by NSF grants EAR-1624178; NSFC grants 41574089 and 41774096.

Data Availability Statement: The data for this study are available from the Brown Digital Repository (https://doi.org/10.26300/g0wk-ty19).

Acknowledgments: This work is benefited greatly from discussions with Reid Cooper, Terry Tullis, Yuval Boneh, Eric Burdette, Nir Badt, Leif Tokle, and Pamela Speciala at Brown University. We appreciate Seth Krukenburg for providing access to EBSD at Boston College, and Kevin Robertson for providing access to FTIR at Brown University. We thank Yongsheng Zhou, Xi Ma and Jiaxiang Dang for providing help with EBSD at the Institute of geology China Earthquake Administration.

Conflicts of Interest: The authors declare no conflict of interest.

References

1. Kelemen, P.B.; Dick, H.J.B. Focused melt flow and localized deformation in the upper mantle: juxtaposition of replacive dunite and ductile shear zones in the Josephine peridotite, SW Oregon. *Journal of Geophysical Research* **1995**, *100*, 423–438, doi:10.1029/94JB02063.
2. Holtzman, B.K.; Groebner, N.J.; Zimmerman, M.E.; Ginsberg, S.B.; Kohlstedt, D.L. Stress-driven melt segregation in partially molten rocks. *Geochemistry, Geophysics, Geosystems* **2003**, *4*, 8607, doi:10.1029/2001GC000258.
3. Takei, Y.; Holtzman, B.K. Viscous constitutive relations of solid-liquid composites in terms of grain boundary contiguity: 1. Grain boundary diffusion control model. *Journal of Geophysical Research* **2009**, *114*, B06205, doi:10.1029/2008JB005850.
4. Holtzman, B.K.; Kohlstedt, D.L.; Zimmerman, M.E.; Heidelbach, F.; Hiraga, T.; Hustoft, J. Melt segregation and strain partitioning: Implications for seismic anisotropy and mantle flow. *Science* **2003**, *301*, 1227–1230, doi:10.1126/science.1087132.
5. King, D.S.H.; Zimmerman, M.E.; Kohlstedt, D.L. Stress-driven Melt Segregation in Partially Molten Olivine-rich Rocks Deformed in Torsion. *Journal of Petrology* **2010**, *51*, 21–42, doi:10.1093/petrology/egp062.
6. Qi, C.; Kohlstedt, D.L.; Katz, R.F.; Takei, Y. Experimental test of the viscous anisotropy hypothesis for partially molten rocks. **2015**, *112*, 1–5, doi:10.1073/pnas.1513790112.
7. Qi, C.; Kohlstedt, D.L. Influence of Compaction Length on Radial Melt Segregation in Torsionally Deformed Partially Molten Rocks. *Geochemistry, Geophysics, Geosystems* **2018**, *19*, 4400–4419, doi:10.1029/2018GC007715.
8. Takei, Y.; Katz, R.F. Consequences of viscous anisotropy in a deforming, two-phase aggregate. Part 1. Governing equations and linearized analysis. *Journal of Fluid Mechanics* **2013**, *734*, 424–455, doi:10.1017/jfm.2013.482.
9. Katz, R.F.; Takei, Y. Consequences of viscous anisotropy in a deforming, two-phase aggregate. Part 2. Numerical solutions of the full equations. *Journal of Fluid Mechanics* **2013**, *734*, 456–485, doi:10.1017/jfm.2013.483.
10. Qi, C.; Hansen, L.N.; Wallis, D.; Holtzman, B.K.; Kohlstedt, D.L. Crystallographic Preferred Orientation of Olivine in Sheared Partially Molten Rocks: The Source of the "a-c Switch." *Geochemistry, Geophysics, Geosystems* **2018**, *19*, 316–336, doi:10.1002/2017GC007309.
11. Mainprice, D. Seismic Anisotropy of the Deep Earth from a Mineral and Rock Physics Perspective. *Treatise on Geophysics* **2007**, *2*, 437–491, doi:10.1016/B978-044452748-6.00045-6.
12. Hirth, G.; Kohlstedt, D.L. Experimental constraints on the dynamics of the partially molten upper mantle: deformation in the diffusion creep regime. *Journal of Geophysical Research* **1995**, *100*, 1981–2001, doi:10.1029/94JB02128.
13. Mei, S.; Bai, W.; Hiraga, T.; Kohlstedt, D.L. Influence of melt on the creep behavior of olivine-basalt aggregates under hydrous conditions. *Earth and Planetary Science Letters* **2002**, *201*, 491–507, doi:10.1016/S0012-821X(02)00745-8.
14. Holtzman, B.K.; King, D.S.H.; Kohlstedt, D.L. Effects of stress-driven melt segregation on the viscosity of rocks. *Earth and Planetary Science Letters* **2012**, *359–360*, 184–193, doi:10.1016/j.epsl.2012.09.030.
15. Bulau, J.R.; Waff, H.S.; Tyburczy, J.A. Mechanical and thermodynamic constraints on fluid distribution in partial melts. *Journal of Geophysical Research* **1979**, *84*, 6102, doi:10.1029/jb084ib11p06102.
16. Waff, H.S.; Bulau, J.R. Equilibrium fluid distribution in an ultramafic partial melt under hydrostatic stress conditions. **1979**, *84*.
17. Cooper, R.F.; Kohlstedt, D.L. Interfacial energies in the olivine basalt system. *High-pressure research in geophysics* **1982**, 217–228, doi:10.1007/978-94-009-7867-6_17.
18. Raj, R. Creep in polycrystalline aggregates by matter transport through a liquid phase. *Journal of Geophysical Research* **1982**, *87*, 4731–4739, doi:10.1029/JB087iB06p04731.
19. Cooper, R.F.; Kohlstedt, D.L. Rheology and structure of olivine-basalt partial melts. *Journal of Geophysical Research* **1986**, *91*, 9315, doi:10.1029/jb091ib09p09315.

Preprints (www.preprints.org) | NOT PEER-REVIEWED | Posted: 12 April 2021 doi:10.20944/preprints202104.0319.v1

20. Bruce Watson, E.; Brenan, J.M. Fluids in the lithosphere, 1. Experimentally-determined wetting characteristics of CO2H2O fluids and their implications for fluid transport, host-rock physical properties, and fluid inclusion formation. *Earth and Planetary Science Letters* **1987**, *85*, 497–515, doi:10.1016/0012-821X(87)90144-0.
21. Heidaryan, E.; Hatami, T.; Rahimi, M.; Moghadasi, J. Viscosity of pure carbon dioxide at supercritical region: Measurement and correlation approach. *Journal of Supercritical Fluids* **2011**, *56*, 144–151, doi:10.1016/j.supflu.2010.12.006.
22. Yoshino, T.; Mcisaac, E.; Laumonier, M.; Katsura, T. Electrical conductivity of partial molten carbonate peridotite. *Physics of the Earth and Planetary Interiors*, **2012,** *194–195*, 1–9. https://doi.org/10.1016/j.pepi.2012.01.005
23. Sleep, N.H.; Zahnle, K. Carbon dioxide cycling and implications for climate on ancient Earth. *Journal of Geophysical Research E: Planets* **2001**, *106*, 1373–1399, doi:10.1029/2000JE001247.
24. Dasgupta, R.; Hirschmann, M.M. The deep carbon cycle and melting in Earth's interior. *Earth and Planetary Science Letters* **2010**, *298*, 1–13, doi:10.1016/j.epsl.2010.06.039.
25. Hirschmann, M.M. Partial melt in the oceanic low velocity zone. *Physics of the Earth and Planetary Interiors* **2010**, *179*, 60–71, doi:10.1016/j.pepi.2009.12.003.
26. Zhao, N.; Hirth, G.; Cooper, R.F.; Kruckenberg, S.C.; Cukjati, J. Low viscosity of mantle rocks linked to phase boundary sliding. *Earth and Planetary Science Letters* **2019**, *517*, 83–94, doi:10.1016/j.epsl.2019.04.019.
27. Jin, Z.-M.; Green, H.W.; Borch, R.S. Microstructures of olivine and stresses in the upper mantle beneath Eastern China. *Tectonophysics* **1989**, *169*, 23–50, doi:10.1016/0040-1951(89)90181-9.
28. Proctor, B.; Hirth, G. Role of pore fluid pressure on transient strength changes and fabric development during serpentine dehydration at mantle conditions: Implications for subduction-zone seismicity. *Earth and Planetary Science Letters* **2015**, *421*, 1–12, doi:10.1016/j.epsl.2015.03.040.
29. Bystricky, M.; Heidelbach, F.; Mackwell, S. Large-strain deformation and strain partitioning in polyphase rocks: Dislocation creep of olivine-magnesiowüstite aggregates. *Tectonophysics* **2006**, *427*, 115–132, doi:10.1016/j.tecto.2006.05.025.
30. Hansen, L.N.; Zimmerman, M.E.; Kohlstedt, D.L. Grain boundary sliding in San Carlos olivine : Flow law parameters and crystallographic - preferred orientation. **2011**, *116*, 1–16, doi:10.1029/2011JB008220.
31. Bachmann, F., Hielscher, R., and Schaeben, H.: Grain detection from 2d and 3d EBSD data–Specification of the MTEX algorithm, *Ultramicroscopy*, **2011**, *111*, 1720–1733,
32. Heilbronner, R.; Barrett, S. Image analysis in earth sciences: Microstructures and textures of earth materials. *Image Analysis in Earth Sciences: Microstructures and Textures of Earth Materials* **2014**, 1–520, doi:10.1007/978-3-642-10343-8.
33. Bachmann, F.; Hielscher, R.; Schaeben, H. Texture analysis with MTEX- Free and open source software toolbox. *Solid State Phenomena* **2010**, *160*, 63–68, doi:10.4028/www.scientific.net/SSP.160.63.
34. Mainprice, D.; Bachmann, F.; Hielscher, R.; Schaeben, H.; Lloyd, G.E. Calculating anisotropic piezoelectric properties from texture data using the MTEX open source package. *Geological Society Special Publication* **2015**, *409*, 223–249, doi:10.1144/SP409.2.
35. Bunge, H.-J. Mathematical Aids. *Texture Analysis in Materials Science* **1982**, 351–403, doi:10.1016/b978-0-408-10642-9.50019-2.
36. Skemer, P.; Katayama, I.; Jiang, Z.; Karato, S.I. The misorientation index: Development of a new method for calculating the strength of lattice-preferred orientation. *Tectonophysics* **2005**, *411*, 157–167, doi:10.1016/j.tecto.2005.08.023.
37. Dasgupta, R.; Hirschmann, M.M.; Smith, N.D. Partial Melting Experiments of Peridotite þ CO 2 at 3 GPa and Genesis of Alkalic Ocean Island Basalts. **2007**, *48*, 2093–2124, doi:10.1093/petrology/egm053.
38. Wyllie, P.J.; Huang, W.L. Influence of mantle CO2 in the generation of carbonatites and kimberlites. *Nature* **1975**, *257*, 297–299, doi:10.1038/257297a0.
39. Dalton, J.A.; Presnall, D.C. Carbonatitic melts along the solidus of model lherzolite in the system CaO-MgO-Al2O3-SiO2-CO2 from 3 to 7 GPa. *Contributions to Mineralogy and Petrology* **1998**, *131*, 123–135, doi:10.1007/s004100050383.
40. Keshav, S.; Gudfinnsson, G.H. Silicate liquid-carbonatite liquid transition along the melting curve of model, vapor-saturated peridotite in the system CaO-MgO-Al2O 3-SiO2-CO2 from 1.1 to 2 GPa. *Journal of Petrology* **2013**, *118*, 3341–3353, doi:10.1002/jgrb.50249.
41. Zhang, Z.; Karato, S. Lattice preferred orientation of olivine aggregates in simple shear", journal = nature. *Nature* **1995**, *375*, 774–777.
42. Miyazaki, T.; Sueyoshi, K.; Hiraga, T. Olivine crystals align during diffusion creep of Earth's upper mantle. *Nature* **2013**, *502*, 321–326, doi:10.1038/nature12570.
43. Donaldson, C.H. An experimental investigation of olivine morphology. *Contributions to Mineralogy and Petrology* **1976**, *57*, 187–213, doi:10.1007/BF00405225.
44. Holtzman, B.K.; Kohlstedt, D.L.; Morgan, J.P. Viscous Energy Dissipation and Strain Partitioning in Partially Molten Rocks. *Journal of Petrology* **2005**, *46*, 2569–2592, doi:10.1093/petrology/egi065.
45. Boneh, Y.; Wallis, D.; Hansen, L.N.; Krawczynski, M.J.; Skemer, P. Oriented grain growth and modification of 'frozen anisotropy' in the lithospheric mantle. *Earth and Planetary Science Letters* **2017,** 474, 368–374, doi:10.1016/j.epsl.2017.06.050.
46. von Bargen, N.; & Waff, H. S. Permeabilities, interfacial areas and curvatures of partially molten systems: Results of numerical computations of equilibrium microstructures. *Journal of Geophysical Research*, **1986**, 91(B9), 9261. https://doi.org/10.1029/jb091ib09p09261